Responses of Coastal Upwelling to Tidally Induced Bottom Friction Dynamics and Plume-Modulated Geostrophy: A Process-Oriented Modeling Study

WEICONG CHENG[a] AND JIANPING GAN[a]

[a] *Department of Ocean Science and Mathematics, Hong Kong University of Science and Technology, Hong Kong, and Southern Marine Science and Engineering Guangdong Laboratory (Zhuhai), Zhuhai, China*

(Manuscript received 9 February 2022, in final form 16 October 2022)

ABSTRACT: We used a high-resolution cross-shelf two-dimensional numerical model to investigate the response of coastal wind-driven upwelling circulation to barotropic tidal forcing and lateral buoyant discharge over a broad continental shelf. We found that the tidally amplified asymmetric friction effect arising from the interaction between tidal and subtidal currents modulated the upwelling structure across the shelf. The interaction weakened the water outcropping (upwelling) in the inner shelf due to tidally amplified mixing, but enhanced cross-shore velocity offshore due to tidally induced asymmetric friction effect and nonlinear advection. The enhanced mixing changed the density in the bottom boundary layer and subsequently in the upwelling front, which eventually weakened the geostrophic alongshore flow. The mass and stratification inputs of the lateral buoyant discharge weakened or even reversed geostrophic dynamics for alongshore and upslope transports. The reversed cross-shore density and elevation gradient induced by the buoyant influx weakened the alongshore current and the associated bottom friction effect. The upslope cross-shore transport was reduced due to weakened alongshore flow and the associated bottom Ekman transport. The mass of buoyant influx compensated for the wind-driven offshore transport in the upper layer. The upwelling could be reversed to downwelling when the transport of lateral influx exceeded the wind-driven offshore transport. The responses of upwelling circulation to tidal and lateral buoyancy forcing highlighted in this process-oriented study are fundamental for interpreting more complex wind-driven shelf circulation.

KEYWORDS: Upwelling/downwelling; Tides; Buoyancy; Coastal flows

1. Introduction

Coastal ocean dynamics are mainly governed by the dynamics of a wind-driven current interacting with shelf topography. Involved with the complex boundary layer (BL) diffusion and advection dynamics (Garrett et al. 1993; Trowbridge and Lentz 1991), the alongshore and cross-shelf circulations and transports respond uniquely to different shelf geometry (Allen et al. 1995), which may be further modulated by the plume and tidal dynamics.

The characteristics of the wind-driven upwelling circulation over the shelf change with Burger number ($S = \alpha N/f$, where α is the bottom slope, N is the buoyancy frequency, and f is the Coriolis parameter). For example, the bottom boundary layer (BBL) over a broad shelf (or small S) develops more quickly compared to a BBL over a steep shelf (or stronger S). The magnitude of the bottom stress is larger over a broad shelf and closer to the value of the wind stress, which induces a larger fraction of the onshore bottom flow and limits the acceleration of an alongshore upwelling jet (Allen et al. 1995; Lentz and Chapman 2004). On the other hand, a well-mixed turbulent inner shelf forms when the surface boundary layer (SBL) overlaps the BBL (Lentz 1995), shutting down the cross-shore transport and leading to divergence in the cross-shore direction (Austin and Lentz 2002; Estrade et al. 2008; Kirincich 2005). The bottom dense water outcrops to the surface within the inner shelf and generates a cross-shore density front and alongshore geostrophic jet. Mixing and stratification intensity is important to the development of the BLs (Lentz and Trowbridge 1991; Taylor and Sarkar 2008) in the inner shelf, and to cross-shore transport near shore (Lentz 2001).

Tidal forcing alters coastal mixing, and, thus, upwelling dynamics. Tidal currents interact with the topography and generate a net cross-shore transport (Chegini et al. 2018; Gu et al. 2012; Tee et al. 1993). Tidally enhanced mixing can directly mix the deep cold water into the surface layer (Jiang et al. 2011; Wang et al. 2015), or set up a baroclinic pressure gradient force near the tidal mixing front to drive the offshore (onshore) flow at the surface (bottom) (Li et al. 2020; Lü et al. 2006). Similarly, a two-dimensional study by Castelao et al. (2010) showed that tidal forcing enhanced mixing within the inner shelf and decreased the cross-shore transport near the coast due to offshore extension of the inner shelf. These studies focus on the effects of the enhanced subtidal mixing, while the intratidal interactions between the tidal currents and background upwelling circulation have seldom been discussed. The intratidal varying interactions affect not only the density mixing but also the momentum balance within the BLs, and subsequently change the subtidal upwelling circulation.

Buoyant discharge enhances stratification within the surface layer and shoals the SBL (Fong and Geyer 2001; Lentz 2001). The buoyant discharge also encourages the SBL and BBL to separate in the nearshore region and leads to a more developed cross-shore Ekman transport (Lentz 2004). The plume-enhanced stratification confines the wind energy and surface Ekman offshore transport within the SBL and strengthens the offshore velocity, while not changing the compensated onshore transport and velocity within the BBL (Gan et al. 2009a). At the head of the alongshore spreading plume, the alongshore density gradient

Corresponding author: Jianping Gan, magan@ust.hk

DOI: 10.1175/JPO-D-22-0037.1

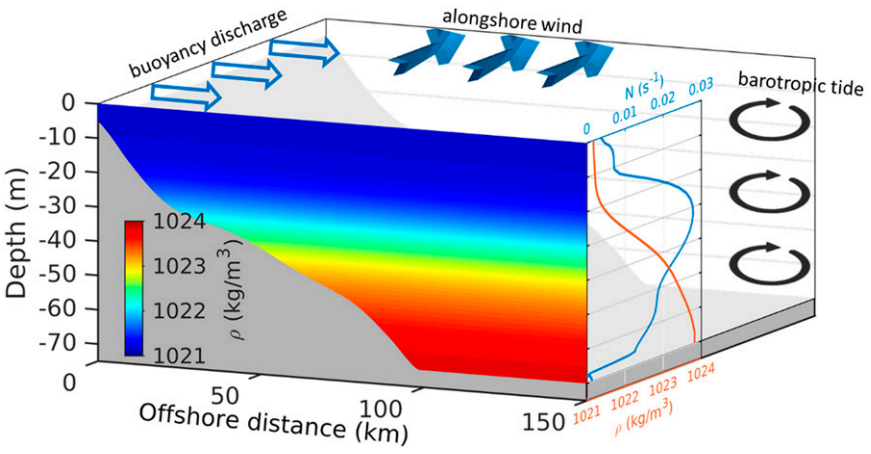

FIG. 1. Initial density field (colored shading) along a cross-shore section and the vertical profiles of initial density (ρ) and buoyancy frequency (N). Arrows schematically represent the different external forcings.

generates geostrophic cross-shore flow and enhances cross-shore transport (Chen et al. 2019). For alongshore circulation, the lateral pressure gradient between the plume and ambient seawater geostrophically accelerates (decelerates) the velocity of the wind-driven currents on the shore side (offshore side) of the plume (Chen et al. 2019; Gan et al. 2009a). These studies focused on the wind–plume interactions in the far field of the lateral buoyancy source, where the buoyancy alters the mixing processes or thermal-wind dynamics. Close to the source area, the persistent influx of buoyant water will cap the upwelled dense water. The outcropping of the upwelled water rather than the upwelling circulation dynamics associated with buoyant influx was addressed in previous studies (Chao 1987; Hickey et al. 2005; Wang et al. 2015; Wang et al. 2012; Wang and Yin 2021; Whitney and Garvine 2005). Besides the buoyancy alteration, the mass influx also leads to the geostrophic response of the shelf current in the near-source area. How the persistent lateral buoyant influx changed mixing and geostrophic alteration influences BL dynamics in the near-source area, and subsequently, the upwelling cross-shore and alongshore circulation is a subject for further research.

The broad shelf in the northern South China Sea (NSCS) is an outstanding example of a coastal sea (Gan et al. 2009a; Zu and Gan 2015) where the wind-driven upwelling circulation interacts with tidal forcing and a large amount of freshwater from the Pearl River Estuary (PRE) during the summer. These interactions play an important role in the cross-shelf exchange of terrestrial and oceanic materials in the coastal area and influence the local biogeochemical processes. In this study, based on the situations of the NSCS, we conducted a process-oriented modeling study to investigate the intrinsic response of the upwelling circulation to tidal forcing and lateral buoyant influx over a broad shelf. We focused on the issues of 1) how the oscillating tidal currents interact with the upwelling circulation, modulate the mixing processes within the BLs, and subsequently change the subtidal upwelling circulation; and 2) responses of the alongshore and cross-shore circulations to the buoyancy and mass alteration from the persistent lateral buoyant input.

2. Model configuration

We adopted the Regional Ocean Modeling System (ROMS; Shchepetkin McWilliams 2005) for our numerical study. ROMS is a primitive equation dynamic model with mixing determined by the MY2.5 turbulent closure scheme (Mellor and Yamada 1982). We configured a two-dimensional (2D) cross-shelf model that had already been widely used in other process-oriented shelf circulation studies (e.g., Allen et al. 1995; Austin and Lentz 2002; Castelao et al. 2010; Estrade et al. 2008; Lentz 1995; Lentz and Chapman 2004). In this classic process-oriented modeling study, we included tidal and lateral buoyant forcing to identify how complex the responses of the upwelling circulation and BL dynamics were. Although our model was simplified, the 2D model isolated the individual processes in the responses and identified the complex interactions, which might not have been feasible with a more complex three-dimensional (3D) rendering.

Cartesian coordinates were introduced with the x axis directed offshore and z axis upward, leaving the y axis in the same direction as the upwelling favorable wind (UFW) in the Northern Hemisphere. The horizontal grid resolution of our simple model was 200 m, and the model had 50 terrain-following vertical levels on sigma coordinates. The resolution near the surface and the bottom was higher than in the middle so that we could better resolve the respective boundary layers. We configured the model's bathymetry from a cross-shelf topography profile over the shelf outside the PRE. We set the minimum depth as 5 m at the shore, and the depth gradually increased to 70 m over a distance of about 100 km (Fig. 1). We extended the model domain 50 km farther offshore with a uniform depth of 70 m to avoid influence from the open offshore boundary. At the open boundary, the surface elevation satisfied an implicit gravity wave radiation condition (Chapman 1985), and the depth-averaged velocity satisfied a Flather radiation scheme (Davies and Flather 1978). We

used radiation boundary conditions (Marchesiello et al. 2001) for the depth-dependent velocities, temperature, and salinity.

We initialized the model with temperature and salinity profiles obtained from field measurements over the shelf of the NSCS. The profiles typified summer conditions in the region (Gan et al. 2009b). The vertical density profile and cross-shore distribution are shown in Fig. 1. We estimated the bottom stress using a quadratic formula with a drag coefficient of $C_d = 2.5 \times 10^{-3}$. We defined the constant Coriolis parameter to be $f = 5.45 \times 10^{-5}$ s^{-1} with an inertial period $T_{\text{ini}} = 2\pi/f = 32$ h for a latitude of 22°, which is the latitude of the PRE. The initial elevation and velocity of the model were zero. Taking the depth-mean buoyancy frequency (N) to be 0.02 s^{-1} and with the mean slope $\alpha = 0.65 \times 10^{-3}$, the Burger number was estimated to be $S = \alpha N/f \approx 0.24$. In this case, the bottom stress plays a dominant role in balancing the surface wind stress in the alongshore momentum balance (Lentz and Chapman 2004).

In line with the objectives of our process-oriented study, we focused on numerical experiments with different external forcings to investigate how the upwelling circulation would respond to 1) wind, 2) tidal forcing, and 3) lateral buoyant flux. The experiments included a baseline case with upwelling favorable wind (UFW) forcing (Case W) for which we applied a steady and spatially uniform along-shelf wind stress (τ_{sy}) of 0.025 Pa (Gan et al. 2009b) over the whole domain. Over the shelf of the NSCS, irregular semidiurnal constituents dominate the tides, and the peak depth-mean tidal currents are 0.2–0.6 m s^{-1}, varying from neap tide to spring tide (Mao et al. 2004). To better identify the underlying dynamics of how tides influence upwelling circulation, we applied a barotropic S_1 ($T_{\text{tide}} = 24$ h) tidal current with a semimajor axes equal to 0.3 m s^{-1} at the open boundary in the second experiment as the tidal case (Case WT). The third experiment was a river case (Case WR) where we discharged buoyant water of 30 psu salinity and 28.6°C (the same as the surface temperature of the initial field) from the coast through the whole water column into the model domain. For simplicity, we used a freshwater flux of 40 m^3 s^{-1} ($V_b = 40$ m^3 s^{-1}/200 m= 0.2 m^2 s^{-1}) with no atmospheric fluxes. In this third experiment, the river discharge first entered the domain after 4 days with wind forcing only. Then, the discharge linearly increased from 0 to the desired flux value over 24 h and stayed constant for the rest of the simulation. After the characteristic responses and background physics were identified, additional experiments with different tidal amplitudes and discharge rates were also conducted to verify the results and mechanisms. Unless otherwise noted, all the variables we presented were daily-averaged values (also tidally averaged) so we could extract the subtidal responses.

3. Fundamental response to wind forcing

The characteristics of the wind-driven upwelling circulation over the shelf in Case W are illustrated in Figs. 2a–e. We focused on the region within 70 km of the coast where the active dynamics were (which we define as $D = 70$ km). To identify the response to the forcing, we used the results from the quasi-steady state reached on day 20, when the bottom shear stress and surface wind stress were in the first-order balance over the entire shelf (Lentz and Chapman 2004).

Driven by the UFW, a strong alongshore jet developed with a jet core at $D = 35$ km with maximum velocity $v = 0.47$ m s^{-1} (Fig. 2a). The alongshore flow was mainly geostrophic except within the inner shelf and close to the bottom (Fig. 3), where the surface and bottom stress played an important role in the momentum balance, similar to that found by Allen et al. (1995). The jet core formed strong horizontal and vertical velocity shears. The upwelled bottom water extended onto the inner shelf (shoreside of $D = 8$ km), where the SBL and BBL overlapped due to the shallowness of the water. The outcropping water formed a high-density dome at the surface, with low-density water on both sides of the dome (Fig. 2c). We identified $D = 8$ km as the upwelling front that separated the inner shelf from the middle shelf. The SBL was thickest where the jet was located, and the thickness of the BBL was uniform offshore from the inner shelf. In this study, we identified the turbulent SBL and BBL regions as the points where the vertical viscosity coefficient (K_M) was greater than 10^{-4} m^2 s^{-1} near the surface or the bottom.

Strong upslope and vertical motions occurred in the BBL and SBL, as shown by the transport streamlines (Fig. 2b). We normalized the streamfunction values (Ψ; $u = \partial\Psi/\partial z$ and $w = -\partial\Psi/\partial x$ indicate the cross-shore and vertical velocities, respectively) with the theoretical wind-induced Ekman transport, $V_E = \tau_{sy}/(\rho_0 f) = 0.45$ m^2 s^{-1}, where $\rho_0 = 1025$ kg m^{-3} is the reference density. The cross-shore flow was concentrated within the BLs. Due to the enhanced alongshore bottom stress at the location of the upwelling front (not shown), the frictional onshore transport increased, and was compensated by the locally strengthened offshore transport at the surface layer, which led to the surface offshore transport convergence on the seaward side of the upwelling front and formed the deepened SBL. Seaward of the upwelling front, there was a strong horizontal density gradient that induced a baroclinic pressure gradient force that sustained the alongshore surface jet.

The water was well mixed within the BLs and weakly stratified over the inner shelf due to the continuous upwelling of dense water. There was a strong pycnocline that separated the SBL and BBL (Fig. 2d) shoreward of the jet, which limited the development of the BLs. An undisturbed inviscid middle layer existed on the seaward side of the jet.

In the MY2.5 mixing scheme, the turbulent kinetic energy [TKE; $(1/2)q^2$], the turbulent mixing length scale (l), and the stability coefficient S_m nonlinearly determine K_M ($K_M = qlS_m + K_{M_{\text{background}}}$). The shear production term $\{P_s = K_M[(\partial u/\partial z)^2 + (\partial v/\partial z)^2]\}$ is the source term, and the turbulent dissipation term ($\xi_d = q^3/(B_1 l)$, where B_1 is a constant) and the buoyancy production term ($P_b = K_H N^2$, where K_H is the vertical diffusion coefficient) are the sink terms in the TKE balance, respectively. The value of l is limited by the presence of the physical boundary and vertical stratification (Scully et al. 2011). The strengthened pycnocline above the BBL constrained the developments of the BBL and K_M due to the increased magnitude of P_b along the bottom pycnocline. Within the SBL, the maximum K_M was on the seaward side of the jet (Fig. 2e). Although the velocity vertical shear was

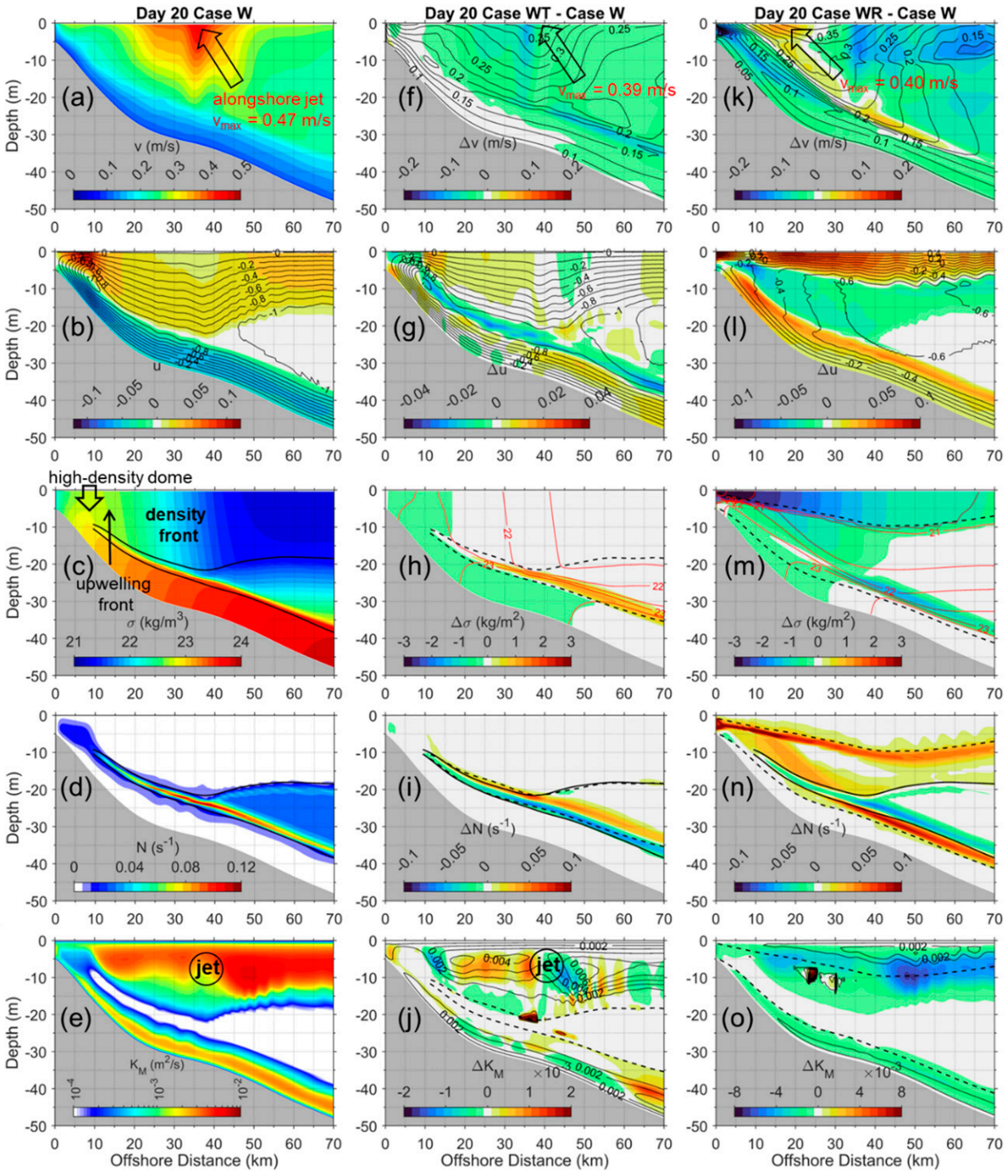

FIG. 2. (left) Day 20 cross-shore distribution of the basic characteristics of Case W, and the influence of (center) the tide and (right) buoyant discharge. (a) Alongshore velocity (v), (b) cross-shore velocity (colored shading) and streamlines (black contour lines; values normalized with the theoretical Ekman transport), (c) density ($\sigma = \rho - 1000$), (d) buoyancy frequency (N), and (e) vertical viscosity (K_M) for Case W. Also shown are (f) alongshore velocity difference between Case WT and Case W (colored shading), and alongshore velocity (black contour lines) of Case WT; (g) cross-shore velocity difference (colored shading) and streamlines (black contour lines) of Case WT; (h) density difference (colored shading) and density (red contour lines) of Case WT; (i) buoyancy frequency difference; (j) vertical viscosity difference (colored shading) and vertical viscosity (black contour lines) of Case WT. (k)–(o) As in (e)–(j), but for Case WR. Black solid lines in (c), (d), (i), and (n) represent the boundaries of the SBL and BBL defined by the intensity of vertical viscosity ($K_M = 10^{-4}$ m^2 s^{-1}) of Case W. Black dashed lines in (h) and (i) and in (m) and (n) represent the boundaries of the SBL and BBL of Case WT and Case WR, respectively.

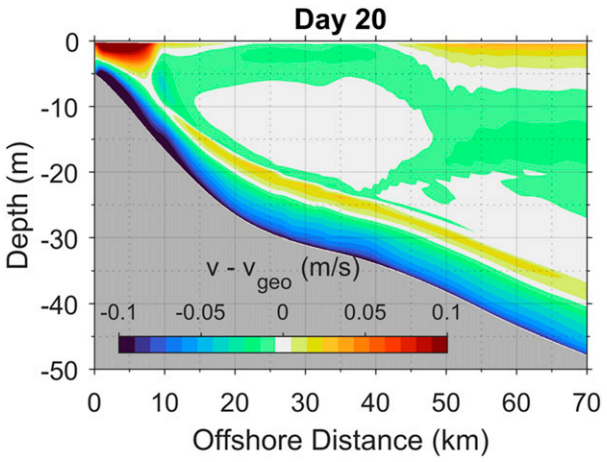

FIG. 3. Cross-shore distribution of the difference between total alongshore velocity and the geostrophic component of Case W on day 20.

stronger (larger P_s) in the inner shelf and below the jet core, the shallow water and strong pycnocline limited l in these two regions, respectively.

These dynamics within the SBL and BBL that we identified for the baseline case were critical to identifying the responses of the upwelling to the tide and lateral buoyant flux in the other two experiments.

4. Effects of tidal forcing

Compared to those in Case W, the barotropic tidal currents weakened the alongshore current (Fig. 2f), decreased the density in the BBL, and decreased the density of the upwelled water (Fig. 2h). Furthermore, the pycnocline above the BBL thickened but its maximum intensity weakened (Fig. 2i). The general structure and magnitude of K_M in Case WT was like that in Case W (Fig. 2j), and we attribute the differences between Case W and Case WT to the seaward shift of the jet. These distinct differences, which we describe in this section, were the response to tidally induced processes, particularly the changes in the density structure because of tidal mixing. We discuss the background physics of these different responses between the two scenarios in section 6.

a. *Weakened geostrophic alongshore jet*

Compared with Case W, the alongshore velocity (v) in Case WT was smaller, especially on the shoreward side of the jet (Fig. 2f). Maximum v was about 0.08 m s^{-1} smaller, and the jet core was farther offshore. To understand the influence of different forcing on the geostrophic alongshore flow, we decomposed the geostrophic flow into barotropic [induced by the cross-shore elevation gradient, $v_{bt} = (g/f)(\partial\eta/\partial x)$] and baroclinic parts ($v_{bc} = -[g/(f\rho_0)]\int_{-h}^{\eta} \partial\rho/\partial x\, dz$). The cross-shore variations of the surface geostrophic velocities are shown in Fig. 4a. Although v_{bc} was one order of magnitude smaller than v_{bt}, these two components varied consistently and reached their maxima at the same location, which indicated an intrinsic link between v_{bc} and v_{bt}. The locations of the surface density front (defined as the location of the maximum negative cross-shore density gradient, $\partial\rho/\partial x$) and the surface jet (Fig. 4b) confirmed that the alongshore velocity was linked to the density field. In Case W and Case WT, the alongshore jet moved offshore with the density front as a result of the surface Ekman offshore transport in the SBL. The enhanced offshore flow within the SBL (Fig. 2g) moved the density front further offshore in Case WT compared to Case W, which led

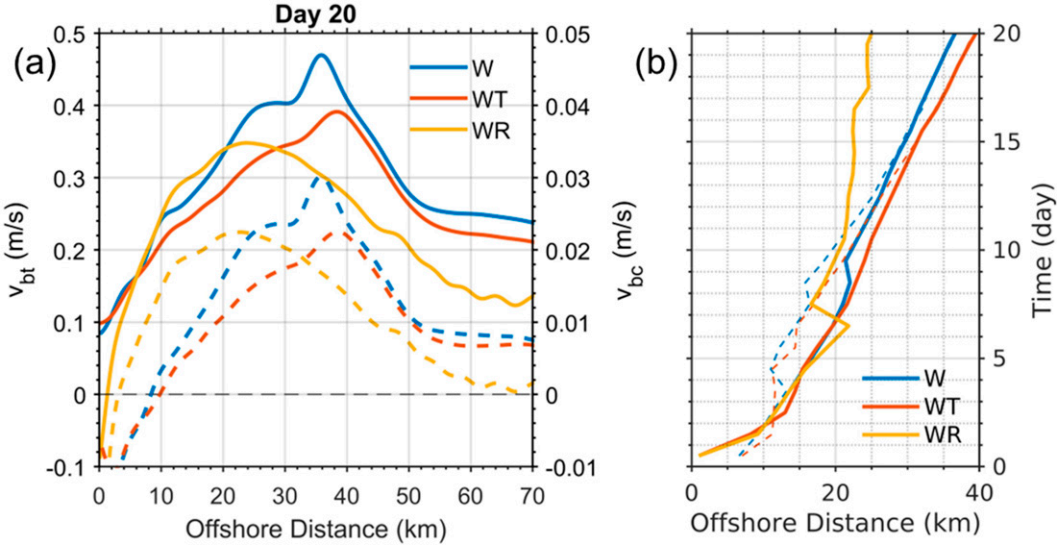

FIG. 4. (a) Barotropic (v_{bt}; solid lines; left y axis) and baroclinic (v_{bc}; dashed lines; right y axis) pressure gradient contributions to the surface alongshore velocity for each case on day 20. The baroclinic velocity component was integrated from the bottom to the surface. (b) Temporal variations of the locations of the surface alongshore jet (solid lines) and surface density front (dashed lines) for the different cases.

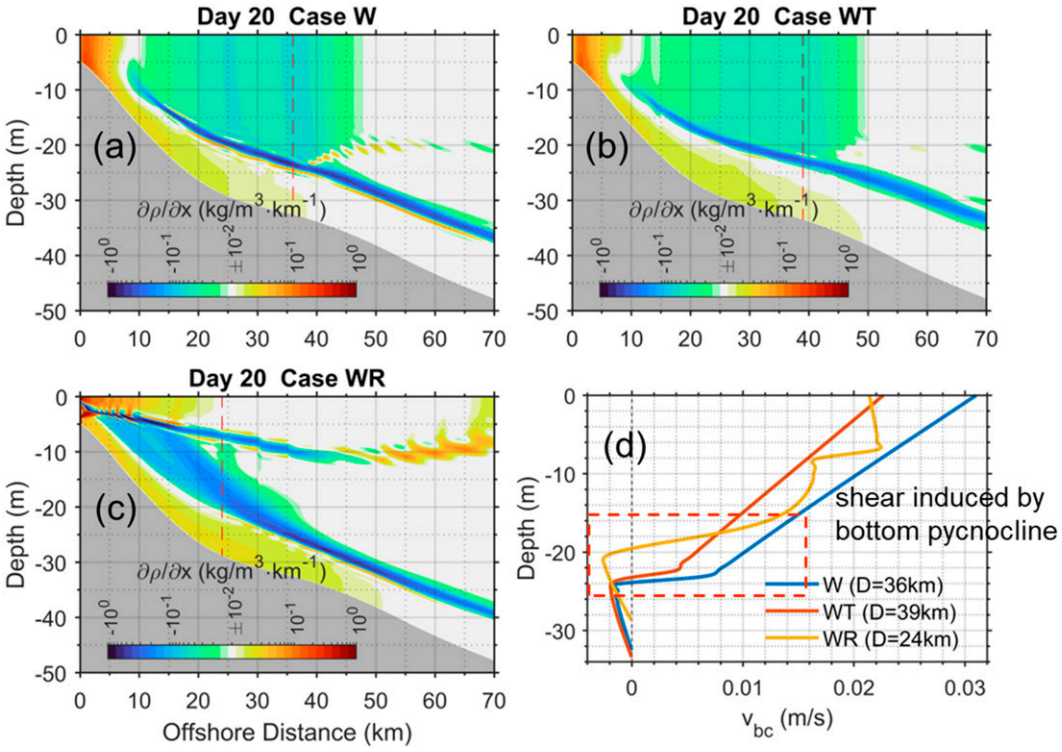

FIG. 5. (a)–(c) Horizontal density gradient for each case on day 20. (d) Vertical profiles of alongshore velocity induced by the baroclinic pressure gradient (v_{bc}) at the jet location of each case on day 20. The jet location of each case is indicated by the vertical red dashed line in (a)–(c).

to the shift in the location of the surface jet when tides were present.

The cross-shore distributions of $\partial\rho/\partial x$ in Case W (Fig. 5a) and Case WT (Fig. 5b) had similar patterns. There was a positive $\partial\rho/\partial x$ within the inner shelf and the BBL, a negative $\partial\rho/\partial x$ within the SBL on the seaward side of the upwelling front, and a much stronger negative $\partial\rho/\partial x$ at the bottom pycnocline to reflect the response to the upwelling. In addition, the gradients were less intense in Case WT.

The vertical profile of the baroclinic velocity component is $v_{bc}(Z) = -[g/(f\rho_0)]\int_{-h}^{Z} \partial\rho/\partial x\, dz$, where Z is the vertical location in the water column. We display $v_{bc}(Z)$ at the location of the surface jet of each case in Fig. 5d to demonstrate the baroclinic effect on the alongshore velocity. Above the BBL, the strong horizontal density gradient from the bottom pycnocline contributed to strong positive vertical shear in v_{bc}, and in the SBL, the negative $\partial\rho/\partial x$ contributed to relatively weak positive velocity shear over a larger vertical extent. In Case WT, the intensity of the bottom pycnocline and horizontal density gradient within the SBL decreased (Figs. 2h,i) due to the enhanced density mixing near the bottom. As a result, the vertical shear of v_{bc} within the whole water column was smaller compared to that in Case W (Fig. 5d), and the total velocity of the alongshore jet varied with v_{bc} (Fig. 4a).

Previous studies (e.g., Kurapov et al. 2010) suggested that the speed of the alongshore velocity in the upwelling circulation can be weaker under the influence of tides because of the smaller tendency term due to the enhanced bottom stress. However, we did not find a significant change in the subtidal bottom stress magnitude, but the tidally enhanced vertical density mixing changed the horizontal density gradient. The weakened cross-shore geostrophic balance reduced the alongshore velocity.

b. *Cross-shore residual flow*

The onshore velocity was slightly weakened in Case WT compared to Case W within the BBL (Figs. 2b,g). Above the BBL, there was significant onshore flow at 10–60 km from shore, which could be attributed to the intratidal friction and nonlinear advection effect (discussed in section 6). The offshore velocity was strengthened within the SBL or above the pycnocline on the seaward side of the upwelling front, moving the density front and associated alongshore jet farther offshore compared to Case W (Fig. 4b).

Since the alongshore pressure gradient is absent in this 2D model, the offshore flux within the SBL should equal the wind-driven Ekman transport [$V_E = \tau_{sy}/(\rho_0 f)$]. However, there was relatively small cross-shore transport close to shore (with the inner shelf at $D < 8$ km) in Case W due to the overlapping SBL and BBL in the shallow water (Austin and Lentz 2002; Estrade et al. 2008) (Fig. 6). In the middle shelf (8 km $< D <$ 40 km in Case W) the cross-shore transport was about 90% of the V_E, because the SBL and BBL were separated by a strong pycnocline (Fig. 2d) and neither BL could be fully developed. Thus, the cross-shore flux was smaller than V_E. Further offshore, when the water was deep

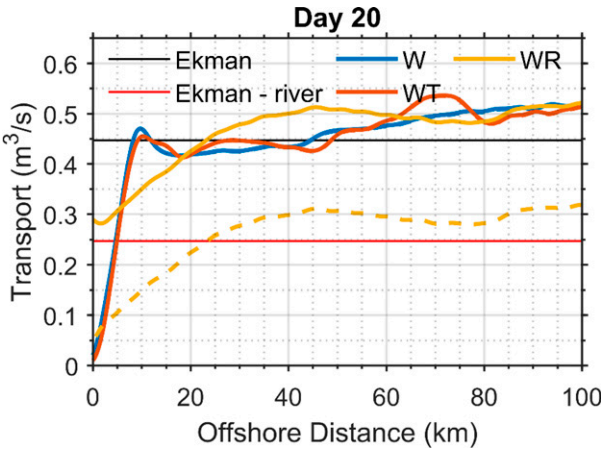

FIG. 6. Cross-shore variations of the offshore transport (solid line)/onshore transport (dashed line) within the SBL/BBL for each case on day 20. The black line represents the value of the theoretical surface Ekman transport. The red line represents the value of the theoretical Ekman transport minus the river discharge rate.

enough for the BLs to fully develop, the cross-shore transport increased and was close to V_E.

The onshore and offshore transport in Case WT were slightly smaller than those in Case W on the shoreward side of $D = 10$ km. In addition, the maximum onshore and offshore transports were located farther offshore due to the extended inner shelf because of the tidally enhanced mixing, which agreed with the results of Castelao et al. (2010). Farther offshore, the onshore velocity in Case WT was smaller but the BBL thickness was larger compared with Case W, making the onshore transport within the BBL similar in both cases. With tidal forcing in Case WT, a stronger surface offshore transport was required to compensate for additional onshore transport induced by the residual onshore flow above the BBL.

In general, tidally enhanced mixing enlarged the inner shelf and weakened the cross-shore transport close to the shore. Seaward of the upwelling front, the tide induced an onshore flux above the BBL and was compensated for by the offshore flux within the SBL, strengthening the cross-shore exchange.

5. Effect of buoyant discharge

The buoyant discharge from the coast weakened the alongshore velocity and shifted the jet core shoreward (Fig. 2k) by decreasing the cross-shore elevation gradient (indicated by v_{bt}, in Fig. 4a). Within $D = 5$ km, v was negative because the buoyant discharge created a strong pressure gradient so that an upwind flow formed. The low-salinity water occupied the surface layer, generating strong stratification between the SBL and the lower layer (Figs. 2m,n), and the thickness of the SBL decreased greatly. The buoyant waters were transported offshore with the advected plume, and the thickness of the freshwater layer increased from the shore to $D = 40$ km but decreased farther offshore, which was similar to the cross-shore structure of the freshwater layer observed by Yankovsky and Voulgaris (2019). Note that K_M was greatly weakened within and below the SBL because of the strong stratification (enhanced P_b) (Figs. 2n,o). The thickness of the BBL also decreased in Case WR because of the weakened alongshore flow, which led to a less developed bottom Ekman layer. Unlike Case W and Case WT, two maximum buoyancy frequencies (pycnoclines) existed at the lower and upper boundaries of the shoaled SBL and BBL (Fig. 2n), respectively. The upwelled water mixed with the buoyant water, and the upwelling density front at the surface, which favored the upwelling alongshore jet, disappeared.

a. Shoreward trap of the jet

The upwelling surface jet in Case WR did not continue to move offshore as in Case W and Case WT (Fig. 4b). Instead, the upwelling surface jet was quasi-stationary by day 10 (5 days after the freshwater discharge input). The two key factors that prevented the offshore migration of the jet were the following. 1) The buoyant flux, particularly at the subsurface, formed a positive $\partial\rho/\partial x$ offshore of $D = 45$ km and constrained the development of the surface velocity, and there was a negative $\partial\rho/\partial x$ shoreward (Fig. 5c). 2) While the wind energy was confined within the SBL, the shoreward tilting pycnoclines above the BBL covered a much larger vertical extent between $D = 5$ and $D = 30$ km and formed a corresponding broad band of negative $\partial\rho/\partial x$ at the subsurface layer with a relatively large contribution of v_{bc} to the total alongshore velocity (Figs. 4a, 5c, and 5d). The positive $\partial\rho/\partial x$ induced by the lateral buoyant water input generated a negative velocity shear near the surface, leaving the maximum alongshore velocity at the subsurface layer.

Gan et al. (2009a) found that freshwater discharge over the shelf in the form of a detached (from the coast) river plume enhances (weakens) the upwelling jet on the shoreward (seaward) side due to a reversed pressure gradient force at the two sides of the plume. In this study, we found that the buoyant water in the source area adhered to the coast. In the source area, the buoyant water raised the water level at the shore side, weakened the alongshore flow by partly canceling the wind-driven cross-shore elevation gradient, and trapped the jet shoreward due to the dual strong $\partial\rho/\partial x$ in the surface and bottom pycnoclines.

b. Weakened upwelling

In Case WR, the wind-driven surface offshore transport was confined to a much thinner SBL, and the velocity was much larger compared to Case W (Fig. 2l). However, the onshore velocity within the thinner BBL decreased. Compared to Case W and Case WT for which the waters upwelled within the narrow inner shelf, the bottom water in Case WR upwelled starting from $D = 25$ km with a much smaller vertical velocity but over a much wider horizontal extent, as the streamlines indicated.

The lateral buoyant discharge changed the magnitude and variation of the cross-shore transport (Fig. 6). The lateral discharge in the source area limited the nearshore BBL and reduced the bottom onshore flow, which shifted the bottom convergence zone offshore, contributing to a wider upwelling

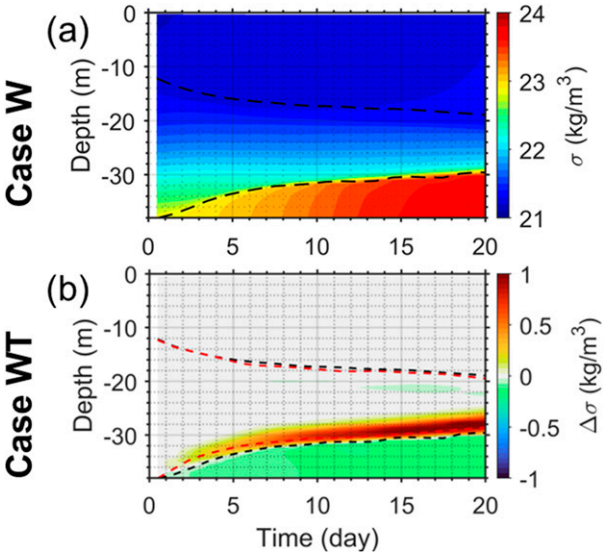

FIG. 7. Temporal variations of density over the whole water column at $D = 50$ km: (a) density (σ) for Case W and (b) the density difference between Case WT and Case W ($\sigma_{WT} - \sigma_W$). Black dashed lines in (a) and (b) represent the boundaries of the SBL and BBL for Case W. Red dashed lines in (b) represent the boundaries of the SBL and BBL for Case WT.

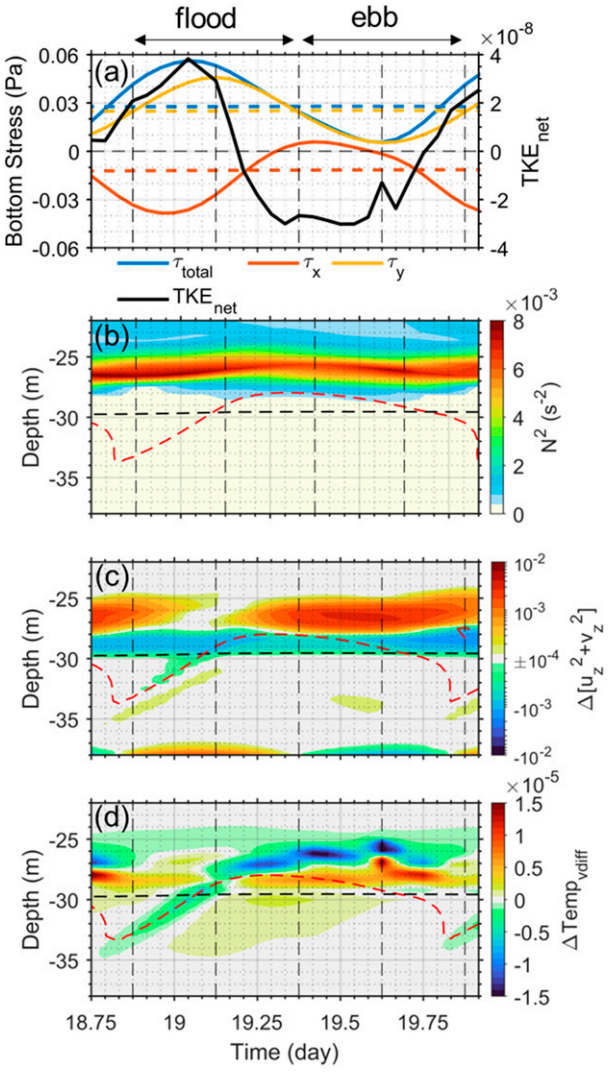

FIG. 8. Intratidal variations of the mixing parameters on day 20 at $D = 50$ km. (a) Bottom stress and net TKE changing rate (TKE_{net}) integrated over the BBL, where the solid lines are for Case WT and the dashed lines are for Case W. The alongshore (τ_y) and cross-shore (τ_x) stresses are plotted in the flow direction. (b) Variation of stratification for Case WT. (c) Difference of velocity shear intensity between Case WT and Case W. (d) Differences of temperature vertical diffusion rate between Case WT and Case W. The horizontal red and black dashed lines in (b)–(d) represent the BBL boundary for Case WT and Case W, respectively.

extent and the stronger tilting of the bottom pycnocline. Shoreward of $D = 25$ km, the cross-shore transports within both BLs were much smaller than that on the seaward side because the onshore transported water upwelled and turned offshore without reaching the shoreward side. Seaward of $D = 25$ km, the surface offshore transport was close to the Ekman transport and larger than that in Case W and Case WT, as the development of the SBL did not interact with the BBL. However, the bottom onshore transport decreased significantly, which was attributed to the weakened alongshore geostrophic flow. The weakened alongshore flow led to the smaller bottom stress and cross-shore Ekman transport. The cross-shore water balance needed to include the additional mass input from the discharge.

Clearly, the response of the wind-driven cross-shore transport to the buoyant flux in the BBL was different from the response in the SBL. The weakened alongshore flow reduced the friction-induced upwelling intensity within the BBL. In the SBL the plume strengthened the stratification, separated the BLs, and favored offshore Ekman transport.

6. Discussion

Without the forcing arising from the alongshore variation of the circulation, the dynamic responses in the SBL and BBL were largely regulated by the upwelling circulation, as the characteristic structures in the BLs show. In Case W, the well-mixed SBL thickened with time, while the BBL reached a quasi-steady state after day 10 due to the onshore dense water transport within the BBL (Fig. 7a). The effects of tide and buoyancy alter these BL dynamics. In this section, we investigate how the intratidal frictional processes within the BBL modulated the subtidal mixing intensity and momentum balance that further regulated the alongshore and cross-shore transport. Then we discuss the characteristic responses of cross-shore geostrophic and density structure, which would modulate the boundary layer dynamics and shelf circulation, to the different discharge rates.

a. Tidally induced bottom frictional dynamics

As we showed in section 4, the water density within (above) the thickened BBL in Case WT was less (greater) than in

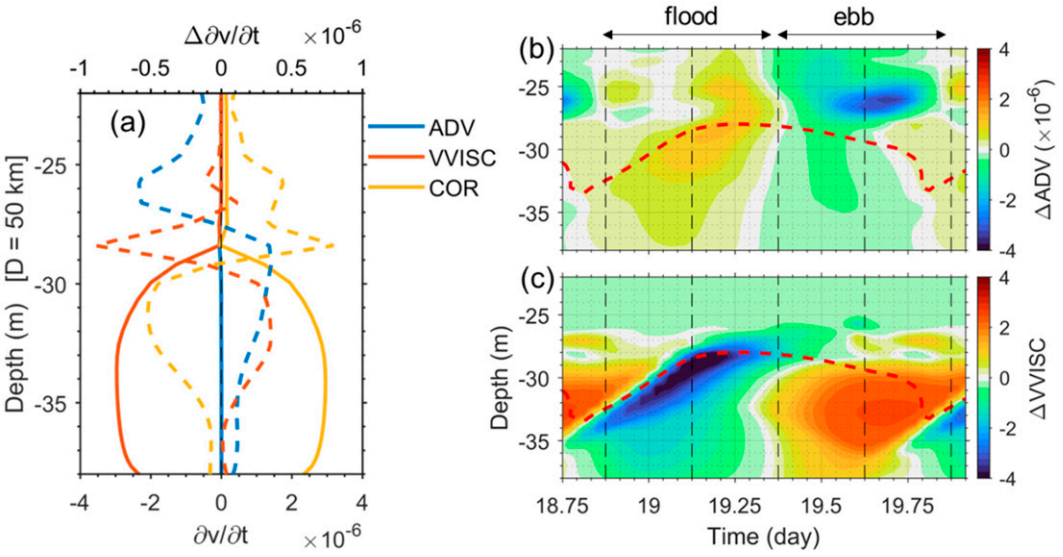

FIG. 9. Comparison of the alongshore momentum terms between Case WT and Case W on day 20 at $D = 50$ km. (a) Daily (tidally) averaged vertical profile of different terms, where the solid lines are for Case W ($\partial v/\partial t$) and the dashed lines show the differences between Case WT and Case W ($\Delta\partial v/\partial t$). Intratidal variations of the differences between the two cases for the (a) total advection term and (b) vertical viscous term. Red dashed lines in (b) and (c) show the boundary of BBL for Case WT.

Case W (Fig. 7b). The intratidal variations of the mixing dynamics are shown in Figs. 8 and 9 to identify the tidal influence on the upwelling dynamics.

In Case WT, we found that the depth-integrated net TKE changing rate ($TKE_{net} = P_S - \xi_d - P_B$) within the BBL (Fig. 8a) was positive at the end of the ebb tide and during most of the flood tide, and negative during the rest of the tidal cycle. The turbulent BBL thickened (thinned) during flood (ebb) tide (Fig. 8b) in response to net TKE generation (dissipation) while the location of the bottom pycnocline was relatively steady (Fig. 8b) and located at a higher location compared with that in Case W. Tide-induced velocity vertical shear was found near the nonslip seabed (referred to as bottom shear) and at the pycnocline bordering the BBL [referred to as interior shear, reported by Werner (2003) and Sakamoto and Akitomo (2009)] (Fig. 8c) but had only a small influence on the SBL (not shown in the figures). During the flood tide, both alongshore and cross-shore bottom stresses were strengthened as the tidal and wind-driven currents were in the same phase (Fig. 8a), and enhanced the bottom shear intensity. The opposite conditions occurred during ebb tide. The vertical location of maximum interior shear followed the pycnocline. Interacting with the wind-driven upwelling circulation, the flood (ebb) currents weakened (enhanced) the interior shear, similar to the results of Fernández-Castro et al. (2018). The combined effect of bottom and interior shear contributed to the variations of TKE_{net} and BBL thickness. The vertical temperature mixing between the BBL and the middle layer was mainly modulated by the interior shear intensity. Temperature vertical diffusion rate was strengthened during the second half of flood tide and during ebb tide (when the interior shear was enhanced) but weakened during the first half of flood tide (Fig. 8d). Overall, the tide-induced mixing decreased (increased) the density within (above) the BBL (Fig. 7b). As a result, a weaker vertical density gradient in the pycnocline above the BBL, and a lower density in the upwelled water occurred in Case WT, as compared to those in Case W (Fig. 2h).

The enhanced subtidal cross-shore transports within SBL and BBL in Case WT were also attributed to the asymmetric intratidal process. Without tidal forcing, the viscous term (VVISC) balanced the Coriolis term ($COR = -fu$ where u is the cross-shore velocity) in the subtidal alongshore momentum balance (Fig. 9a), and the total advection term (ADV) was close to zero. The tide-induced nonlinear advection modulated the momentum balance over the slope (Kurapov et al. 2010). Above the BBL, the magnitude of the negative ADV term during ebb tide was greater than the positive magnitude during flood tide, while the situation reversed within the BBL (Fig. 9b). As a result, the tidally averaged ADV term was negative (positive) above (within) the BBL (Fig. 9a). Furthermore, the negative VVISC term was significantly strengthened in the upper part of the BBL during flood tide but weakened in the middle part of the BBL during ebb tide (Fig. 9c) due to the variation of the bottom stress. Therefore, the subtidal negative VVISC term was weakened (strengthened) above (within) the tidally averaged BBL. In response to the variations of ADV and VVISC terms, the positive COR term was strengthened (weakened) above (within) the BBL. As a result, the intratidal asymmetric friction and nonlinear advection effect intensified (weakened) onshore velocity above (within) the thickened BBL and increased the total subtidal onshore transport on the offshore side of the upwelling front.

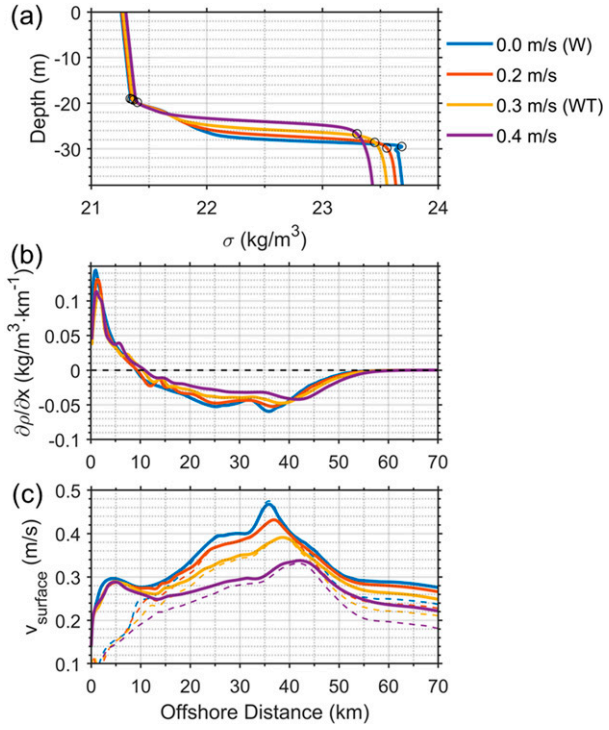

FIG. 10. Responses of upwelling circulation to different amplitudes of tidal current on day 20: (a) density profiles at $D = 50$ km, (b) surface horizontal density gradient, and (c) surface alongshore velocity, where solid lines are the total velocity, and dashed lines are the geostrophic velocity. The black circles in (a) denote the boundaries of the SBL and BBL for each case.

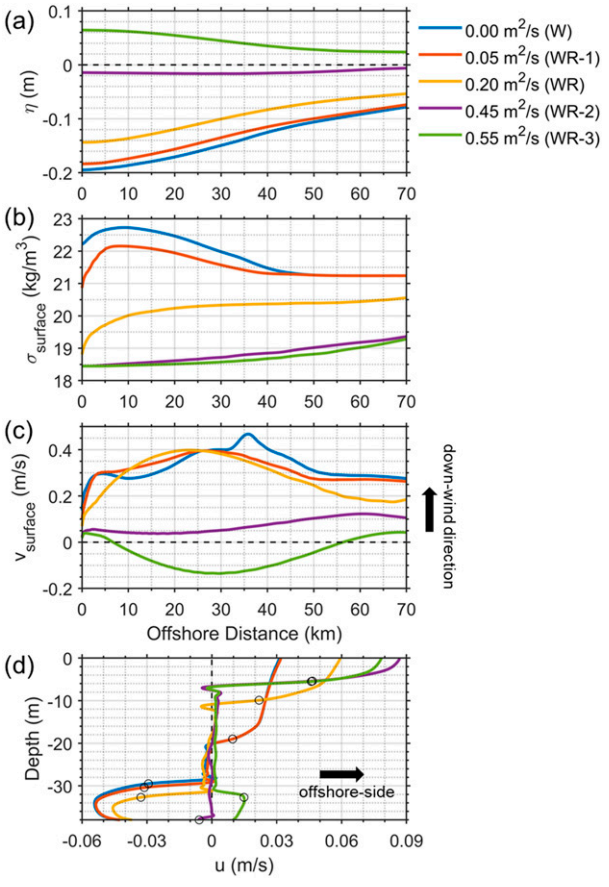

FIG. 11. Responses of the upwelling circulation to different buoyant discharge rates on day 20: (a) elevation, (b) surface density, (c) surface alongshore velocity, and (d) cross-shore velocity profiles at $D = 50$ km. The black circles in (d) denote the boundaries of the SBL and BBL for each case.

Additional experiments with different tidal amplitudes showed that a stronger tidal forcing thickened the BBL (Fig. 10a) and decreased (increased) the density within (above) the BBL, which weakened the intensity of the bottom pycnocline and horizontal density front in the surface (Fig. 10b), and, subsequently, the geostrophic and total alongshore flow (Fig. 10c).

b. Geostrophic modulation by buoyant discharge

The lateral buoyant discharge in Case WR mainly altered the cross-shore density (pressure) and enhanced the stratification that confined the input wind energy to the SBL (Chen et al. 2019; Gan et al. 2009a). Unlike the bottom-advected plume in the buoyancy-only forcing case (Chapman and Lentz 1994), the effects of wind-driven surface-advected buoyant water on BBL dynamics and upwelling circulation were indirect. In our results, the buoyant discharge barotropically modulated alongshore circulation by decreasing the cross-shore elevation gradient (Fig. 4a or Fig. 11a). As a result, the weaker alongshore flow formed a less-developed BBL over the entire shelf compared to Case W. This weakened the bottom onshore flow and upwelling intensity.

The fate of a plume under the influence of ambient shelf flow has received much attention in the literature regarding plume studies. The plume is transported by wind-driven currents, and, in turn, alters the circulation (Chen et al. 2017; García Berdeal et al. 2002; O'Donnell 1990). We expect that the intensity of the circulation alteration varies with the magnitude of the buoyant discharge rate, particularly in the source area. We conducted additional experiments with different buoyant discharge rates (V_b) of 0.05 m^2 s^{-1}, 0.45 m^2 s^{-1} (close to the wind-driven Ekman transport, V_E), and 0.55 m^2 s^{-1}, denoted as Case WR-1, WR-2, and WR-3, respectively. In Case WR-1, with a low discharge rate (about 11% of V_E), there was a negative $\partial\rho/\partial x$ induced by dense upwelled water (Fig. 11b) and an alongshore jet centered at $D = 30$ km (Fig. 11c). The response in WR-1 was qualitatively the same as the response in Case W. In Case WR-2, when V_b was close to V_E, all the discharged waters were transported offshore by surface Ekman transport and flattened cross-shore elevation gradient (Fig. 11a). The geostrophic alongshore flow was almost shut down, and the BBL and the frictional transport were absent (Fig. 11d). Further increasing the discharge rate (Case WR-3) caused the cross-shore pressure gradient to reverse direction, and the alongshore flow turned upwind. In this case, downwelling circulation occurred when the flux of buoyant discharge exceeded the wind-driven offshore flux (Fig. 11d).

The phenomenon that the alongshore flow direction in the nearshore area is determined by the relative intensity of wind stress and buoyant water influx was identified in the South Atlantic Bight with many lateral discharge sources (Kourafalou et al. 1996), and near an estuary with a wide entrance connecting to a coastal shelf, such as the PRE (Chen et al. 2017; Ou 2007; Xu et al. 2019). However, the background mechanism was not clear. This study found that the relative magnitude between the lateral buoyant discharge rates and wind-driven Ekman transport modulated the cross-shore elevation gradient and the intensity/direction of alongshore geostrophic flow in the near-source area.

7. Summary and conclusions

We conducted a process-oriented study to illustrate the different responses of the wind-driven coastal upwelling circulation to two important forcings in a coastal area: tides and buoyant discharge. We utilized an idealized cross-shelf two-dimensional model to isolate the characteristic responses within the BLs, and their influence on the upwelling circulation over a broad shelf (small Burger number) where the bottom stress played an important role and where the dynamics within the SBL and BBL were linked closely in the inner shelf. The schematic pictures in Fig. 12 present our major findings.

The tidal currents changed the vertical shear of velocity not only along the no-slip seabed but also along the bottom pycnocline bordering the turbulent BBL and interior water. The shear intensity and BBL thickness varied with the tidal phase, but overall the tide strengthened density mixing and thickened the BBL (Fig. 12a) but had a negligible influence on the mixing dynamics within the SBL. The enhanced bottom density mixing decreased the intensity of the shoreward tilting bottom pycnocline and lowered the density of the upwelled water, which further decreased the horizontal density gradients within the SBL. The weakened density front and tilting bottom pycnocline baroclinically reduced the geostrophic alongshore flow. For cross-shore circulation, tidal mixing broadened the inner shelf and weakened the corresponding cross-shore transport. Seaward of the upwelling front, the intratidal variations of friction and nonlinear advection effects in the bottom layer formed a residual onshore flow above the BBL. The enhanced onshore transport was compensated for by the enhanced offshore flow within the SBL, which shifted the density front and the alongshore jet farther offshore.

The continuous lateral buoyant influx in the source area greatly modulated the cross-shore pressure (density) gradient and the geostrophic alongshore flow intensity, which changed the frictional Ekman cross-shore flux within the BBL. The additional discharged volume needed to be included in the cross-shore transport balance. Figure 12b shows that when the discharge rate was high enough to reverse the upwelling-induced surface density gradient but lower than the wind-driven Ekman transport, the lateral buoyant discharge weakened the cross-shore pressure gradient and alongshore geostrophic flow created by the upwelling favorable wind, thereby limiting upwelling and BBL development. The buoyant water capped

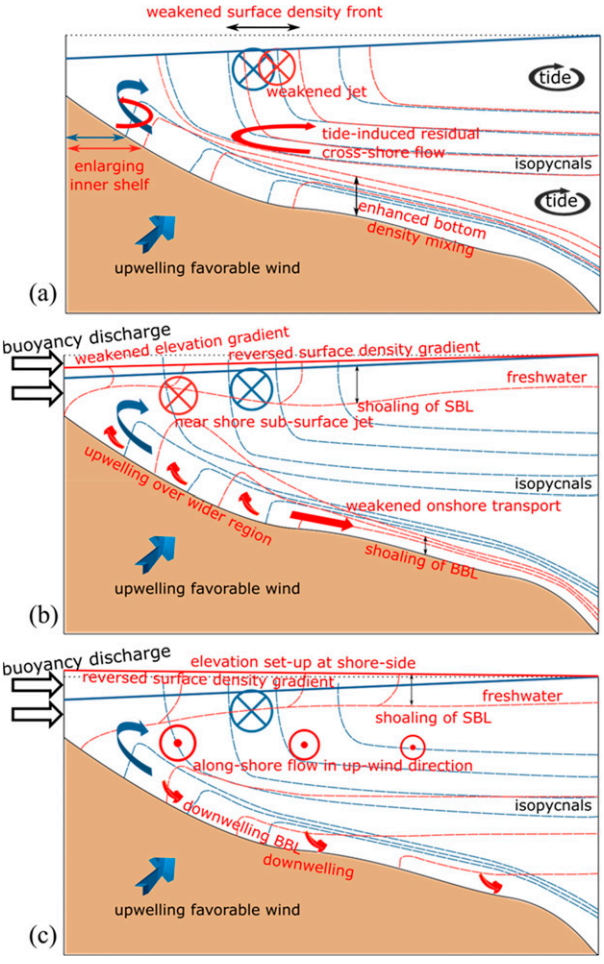

FIG. 12. Schematic representation of the wind-driven upwelling circulation (blue color notations) and responses to (a) tidal forcing, (b) moderate buoyant water input, and (c) large buoyant water input (red color notations). The distinct characteristic responses include enhanced bottom mixing, broadened inner shelf, weakened surface density front, offshore-shifted jet, and strengthened (weakened) cross-shore transport cell on the seaward (shoreward) side of the upwelling front in (a); decreased cross-shore pressure gradient, shoaling of the SBL and BBL, widened upwelling, trapped subsurface jet over the inner shelf, and weakened onshore transport within the BBL in (b); and higher water elevation on the shoreward side, upwind alongshore flow, and downwelling within the BBL in (c).

the signals of the upwelling water, and the density front, which favored the alongshore jet, disappeared. However, as the wind energy was confined to the shoaled SBL, the shoreward tilting pycnoclines generated vertical and horizontal density gradients over a large nearshore extent, sustaining and trapping the subsurface alongshore jet near the coast. If the buoyant discharge rate had been greater than the wind-driven offshore transport (Fig. 12c), the water level would have been higher on the shoreward side and would have generated upwind geostrophic alongshore flow or downwelling circulation.

In conclusion, this process-oriented study enriches the understanding of the dynamics of upwelling circulation and characteristic responses (including the boundary layer dynamics, vertical density mixing, alongshore flow intensity, and cross-shore transport) to the intratidal varying interactions and the buoyancy and mass input from the lateral influx. Knowledge of these factors will contribute to a more accurate and comprehensive interpretation of the physics in wind-driven shelf circulation over any variable shelf under complex forcing.

Acknowledgments. This work was supported by Innovation Group Project of Southern Marine Science and Engineering Guangdong Laboratory (Zhuhai) (projects 311020003 and 311021004), the Theme-based Research Scheme (T21-602/16-R, GRF16212720) of the Hong Kong Research Grants Council. We are grateful for the support of The National Supercomputing Centers of Tianjin and Guangzhou. We are also grateful for the valuable comments provided by the anonymous reviewers.

Data availability statement. The data for this study are generated from the publicly distributed Regional Ocean Model System (ROMS; https://www.myroms.org/).

REFERENCES

Allen, J. S., P. A. Newberger, and J. Federiuk, 1995: Upwelling circulation on the Oregon continental shelf. Part I: Response to idealized forcing. *J. Phys. Oceanogr.*, **25**, 1843–1866, https://doi.org/10.1175/1520-0485(1995)025<1843:UCOTOC>2.0.CO;2.

Austin, J. A., and S. J. Lentz, 2002: The inner shelf response to wind-driven upwelling and downwelling. *J. Phys. Oceanogr.*, **32**, 2171–2193, https://doi.org/10.1175/1520-0485(2002)032<2171:TISRTW>2.0.CO;2.

Castelao, R., R. Chant, S. Glenn, and O. Schofield, 2010: The effects of tides and oscillatory winds on the subtidal inner-shelf cross-shelf circulation. *J. Phys. Oceanogr.*, **40**, 775–788, https://doi.org/10.1175/2009JPO4273.1.

Chao, S.-Y., 1987: Wind-driven motion near inner shelf fronts. *J. Geophys. Res.*, **92**, 3849–3860, https://doi.org/10.1029/JC092iC04p03849.

Chapman, D. C., 1985: Numerical treatment of cross-shelf open boundaries in a barotropic coastal ocean model. *J. Phys. Oceanogr.*, **15**, 1060–1075, https://doi.org/10.1175/1520-0485(1985)015<1060:NTOCSO>2.0.CO;2.

——, and S. J. Lentz, 1994: Trapping of a coastal density front by the bottom boundary layer. *J. Phys. Oceanogr.*, **24**, 1464–1479, https://doi.org/10.1175/1520-0485(1994)024<1464:TOACDF>2.0.CO;2.

Chegini, F., Y. Lu, A. Katavouta, and H. Ritchie, 2018: Coastal upwelling off southwest Nova Scotia simulated with a high-resolution baroclinic ocean model. *J. Geophys. Res. Oceans*, **123**, 2318–2331, https://doi.org/10.1002/2017JC013431.

Chen, Z., W. P. Gong, H. Y. Cai, Y. Z. Chen, and H. Zhang, 2017: Dispersal of the Pearl River plume over continental shelf in summer. *Estuarine Coastal Shelf Sci.*, **194**, 252–262, https://doi.org/10.1016/j.ecss.2017.06.025.

——, Y. W. Jiang, J. Wang, and W. P. Gong, 2019: Influence of a river plume on coastal upwelling dynamics: Importance of stratification. *J. Phys. Oceanogr.*, **49**, 2345–2363, https://doi.org/10.1175/JPO-D-18-0215.1.

Davies, A. M., and R. A. Flather, 1978: Application of numerical models of the Northwest European Continental Shelf and the North Sea to the computation of the storm surges of November to December 1973. Deutsches Hydrographisches Institut, 72 pp.

Estrade, P., P. Marchesiello, A. C. De Verdière, and C. Roy, 2008: Cross-shelf structure of coastal upwelling: A two-dimensional extension of Ekman's theory and a mechanism for inner shelf upwelling shut down. *J. Mar. Res.*, **66**, 589–616, https://doi.org/10.1357/002224008787536790.

Fernández-Castro, B., M. Gilcoto, A. C. Naveira-Garabato, M. Villamaña, R. Graña, and B. Mouriño-Carballido, 2018: Modulation of the semidiurnal cycle of turbulent dissipation by wind-driven upwelling in a coastal embayment. *J. Geophys. Res. Oceans*, **123**, 4034–4054, https://doi.org/10.1002/2017JC013582.

Fong, D. A., and W. R. Geyer, 2001: Response of a river plume during an upwelling favorable wind event. *J. Geophys. Res.*, **106**, 1067–1084, https://doi.org/10.1029/2000JC900134.

Gan, J. P., L. Li, D. X. Wang, and X. G. Guo, 2009a: Interaction of a river plume with coastal upwelling in the northeastern South China Sea. *Cont. Shelf Res.*, **29**, 728–740, https://doi.org/10.1016/j.csr.2008.12.002.

——, A. Cheung, X. G. Guo, and L. Li, 2009b: Intensified upwelling over a widened shelf in the northeastern South China Sea. *J. Geophys. Res.*, **114**, C09019, https://doi.org/10.1029/2007JC004660.

García Berdeal, I., B. M. Hickey, and M. Kawase, 2002: Influence of wind stress and ambient flow on a high discharge river plume. *J. Geophys. Res.*, **107**, 3130, https://doi.org/10.1029/2001JC000932.

Garrett, C., P. MacCready, and P. Rhines, 1993: Boundary mixing and arrested Ekman layers: Rotating stratified flow near a sloping boundary. *Annu. Rev. Fluid Mech.*, **25**, 291–323, https://doi.org/10.1146/annurev.fl.25.010193.001451.

Gu, Y., J. Pan, and H. Lin, 2012: Remote sensing observation and numerical modeling of an upwelling jet in Guangdong coastal water. *J. Geophys. Res.*, **117**, C08019, https://doi.org/10.1029/2012JC007922.

Hickey, B., S. Geier, N. Kachel, and A. MacFadyen, 2005: A bi-directional river plume: The Columbia in summer. *Cont. Shelf Res.*, **25**, 1631–1656, https://doi.org/10.1016/j.csr.2005.04.010.

Jiang, Y., F. Chai, Z. Wan, X. Zhang, and H. Hong, 2011: Characteristics and mechanisms of the upwelling in the southern Taiwan Strait: A three-dimensional numerical model study. *J. Oceanogr.*, **67**, 699–708, https://doi.org/10.1007/s10872-011-0080-x.

Kirincich, A. R., 2005: Wind-driven inner-shelf circulation off central Oregon during summer. *J. Geophys. Res.*, **110**, C10S03, https://doi.org/10.1029/2004JC002611.

Kourafalou, V. H., L.-Y. Oey, J. D. Wang, and T. N. Lee, 1996: The fate of river discharge on the continental shelf: 1. Modeling the river plume and the inner shelf coastal current. *J. Geophys. Res.*, **101**, 3415–3434, https://doi.org/10.1029/95JC03024.

Kurapov, A. L., J. S. Allen, and G. D. Egbert, 2010: Combined effects of wind-driven upwelling and internal tide on the

continental shelf. *J. Phys. Oceanogr.*, **40**, 737–756, https://doi.org/10.1175/2009JPO4183.1.

Lentz, S. J., 1995: Sensitivity of the inner-shelf circulation to the form of the eddy viscosity profile. *J. Phys. Oceanogr.*, **25**, 19–28, https://doi.org/10.1175/1520-0485(1995)025<0019:SOTISC>2.0.CO;2.

——, 2001: The influence of stratification on the wind-driven cross-shelf circulation over the North Carolina shelf. *J. Phys. Oceanogr.*, **31**, 2749–2760, https://doi.org/10.1175/1520-0485(2001)031<2749:TIOSOT>2.0.CO;2.

——, 2004: The response of buoyant coastal plumes to upwelling-favorable winds. *J. Phys. Oceanogr.*, **34**, 2458–2469, https://doi.org/10.1175/JPO2647.1.

——, and J. H. Trowbridge, 1991: The bottom boundary layer over the Northern California Shelf. *J. Phys. Oceanogr.*, **21**, 1186–1201, https://doi.org/10.1175/1520-0485(1991)021<1186:TBBLOT>2.0.CO;2.

——, and D. C. Chapman, 2004: The importance of nonlinear cross-shelf momentum flux during wind-driven coastal upwelling. *J. Phys. Oceanogr.*, **34**, 2444–2457, https://doi.org/10.1175/JPO2644.1.

Li, Y. N., E. N. Curchitser, J. Wang, and S. Q. Peng, 2020: Tidal effects on the surface water cooling northeast of Hainan Island, South China Sea. *J. Geophys. Res. Oceans*, **125**, e2019JC016016, https://doi.org/10.1029/2019JC016016.

Lü, X., F. Qiao, C. Xia, J. Zhu, and Y. Yuan, 2006: Upwelling off Yangtze River estuary in summer. *J. Geophys. Res.*, **111**, C11S08, https://doi.org/10.1029/2005JC003250.

Mao, Q. W., P. Shi, K. D. Yin, J. P. Gan, and Y. Q. Qi, 2004: Tides and tidal currents in the Pearl River estuary. *Cont. Shelf Res.*, **24**, 1797–1808, https://doi.org/10.1016/j.csr.2004.06.008.

Marchesiello, P., J. C. McWilliams, and A. Shchepetkin, 2001: Open boundary conditions for long-term integration of regional oceanic models. *Ocean Modell.*, **3** (1–2), 1–20, https://doi.org/10.1016/S1463-5003(00)00013-5.

Mellor, G. L., and T. Yamada, 1982: Development of a turbulence closure-model for geophysical fluid problems. *Rev. Geophys.*, **20**, 851–875, https://doi.org/10.1029/RG020i004p00851.

O'Donnell, J., 1990: The formation and fate of a river plume: A numerical model. *J. Phys. Oceanogr.*, **20**, 551–569, https://doi.org/10.1175/1520-0485(1990)020<0551:TFAFOA>2.0.CO;2.

Ou, S., 2007: Horizontal characteristics of buoyant plume off the Pearl River estuary during summer. *J. Coastal Res.*, **50** (special issue), 652–657.

Sakamoto, K. E. I., and K. Akitomo, 2009: The tidally induced bottom boundary layer in the rotating frame: Development of the turbulent mixed layer under stratification. *J. Fluid Mech.*, **619**, 235–259, https://doi.org/10.1017/S0022112008004503.

Scully, M. E., W. R. Geyer, and J. H. Trowbridge, 2011: The influence of stratification and nonlocal turbulent production on estuarine turbulence: An assessment of turbulence closure with field observations. *J. Phys. Oceanogr.*, **41**, 166–185, https://doi.org/10.1175/2010JPO4470.1.

Shchepetkin, A. F., and J. C. McWilliams, 2005: The Regional Oceanic Modeling System (ROMS): A split-explicit, free-surface, topography-following-coordinate oceanic model. *Ocean Modell.*, **9**, 347–404, https://doi.org/10.1016/j.ocemod.2004.08.002.

Taylor, J. R., and S. Sarkar, 2008: Stratification effects in a bottom Ekman layer. *J. Phys. Oceanogr.*, **38**, 2535–2555, https://doi.org/10.1175/2008JPO3942.1.

Tee, K. T., P. C. Smith, and D. Lefaivre, 1993: Topographic upwelling off southwest Nova Scotia. *J. Phys. Oceanogr.*, **23**, 1703–1726, https://doi.org/10.1175/1520-0485(1993)023<1703:TUOSNS>2.0.CO;2.

Trowbridge, J. H., and S. J. Lentz, 1991: Asymmetric behavior of an oceanic boundary layer above a sloping bottom. *J. Phys. Oceanogr.*, **21**, 1171–1185, https://doi.org/10.1175/1520-0485(1991)021<1171:ABOAOB>2.0.CO;2.

Wang, D., W. Zhuang, S.-P. Xie, J. Hu, Y. Shu, and R. Wu, 2012: Coastal upwelling in summer 2000 in the northeastern South China Sea. *J. Geophys. Res.*, **117**, C04009, https://doi.org/10.1029/2011JC007465.

Wang, K., and K. Yin, 2021: Barrier effect of the Pearl River estuarine plume on wind-induced coastal upwelling of nutrients. *J. Geophys. Res. Biogeosci.*, **126**, e2020JG006067, https://doi.org/10.1029/2020JG006067.

Wang, Y., Y. Yang, J. Wang, and X. Bai, 2015: A modeling study of the effects of river runoff, tides, and surface wind-wave mixing on the eastern and western Hainan upwelling systems of the South China Sea, China. *Ocean Dyn.*, **65**, 1143–1164, https://doi.org/10.1007/s10236-015-0857-3.

Werner, S. R., 2003: Observations and modeling of the tidal bottom boundary layer on the southern flank of Georges Bank. *J. Geophys. Res.*, **108**, 8005, https://doi.org/10.1029/2001JC001271.

Whitney, M. M., and R. W. Garvine, 2005: Wind influence on a coastal buoyant outflow. *J. Geophys. Res.*, **110**, C03014, https://doi.org/10.1029/2003JC002261.

Xu, C., Y. Xu, J. Hu, S. Li, and B. Wang, 2019: A numerical analysis of the summertime Pearl River plume from 1999 to 2010: Dispersal patterns and intraseasonal variability. *J. Mar. Syst.*, **192**, 15–27, https://doi.org/10.1016/j.jmarsys.2018.12.010.

Yankovsky, A. E., and G. Voulgaris, 2019: Response of a coastal plume formed by tidally modulated estuarine outflow to light upwelling-favorable wind. *J. Phys. Oceanogr.*, **49**, 691–703, https://doi.org/10.1175/JPO-D-18-0126.1.

Zu, T. T., and J. P. Gan, 2015: A numerical study of coupled estuary–shelf circulation around the Pearl River Estuary during summer: Responses to variable winds, tides and river discharge. *Deep-Sea Res. II*, **117**, 53–64, https://doi.org/10.1016/j.dsr2.2013.12.010.